# Supporting Online Material for

High-throughput single nanoparticle detection using a feed-through channel-integrated nanopore

MakusuTsutsui,[1]* Tomoko Yamazaki,[1] Kenji Tatematsu,[1] Kazumichi Yokota,[1,2] Yuko Esaki,[1] Yukari Kubo,[1] Hiroko Deguchi,[1] Shun'ichi Kuroda[1]* & Tomoji Kawai[1]*

[1]The Institute of Scientific and Industrial Research, Osaka University, 8-1 Mihogaoka, Ibaraki, Osaka 567-0047, Japan

[2]National Institute of Advanced Industrial Science and Technology, Takamatsu, Kagawa 761-0395, Japan
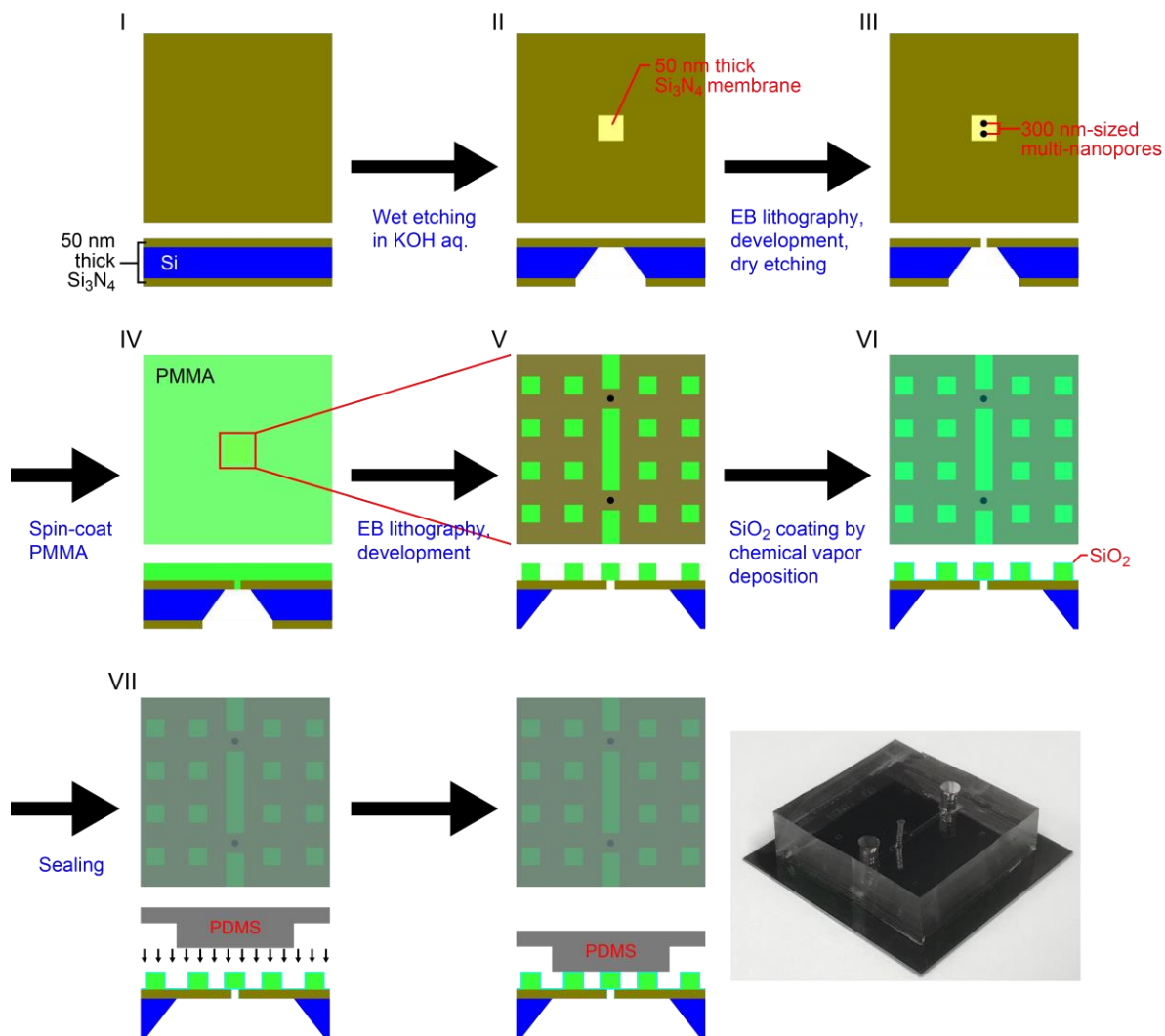
Figure S1. Fabrication processes of a feed-through channel-integrated nanopore. Starting substrate is a piece of 0.3 mm-thick Si wafer both sides coated with 50 nm-thick low-pressure chemical vapour deposition grown Si_3N_4 layers (I). By removing 1 mm square area of Si_3N_4 by reactive ion etching with CF4 etchant gas, the Si layer was wet etched in KOH aq. so as to obtain 50 nm-thick Si3N4 membrane of size approximately 100 μm x 100 μm on the other side (II). On the membrane surface, we delineated multipores of diameter 300 nm

in a spin-coated resist layer (ZEP520A) by a standard electron beam (EB) lithography followed by the dry etching to open the pores (III).   After that, we spin-coated 1 μm-thick polymethyl methacrylate (PMMA; IV) and lithographed pillars and fluidic channels by the EB lithography (V).   Then, the PMMA side of the substrate surface was coated with 20 nm-thick SiO_2 by chemical vapour deposition for making better hydrophilic surface (VI).   Finally, the PMMA/SiO_2 channel was sealed from the top by a PDMS block (VII).
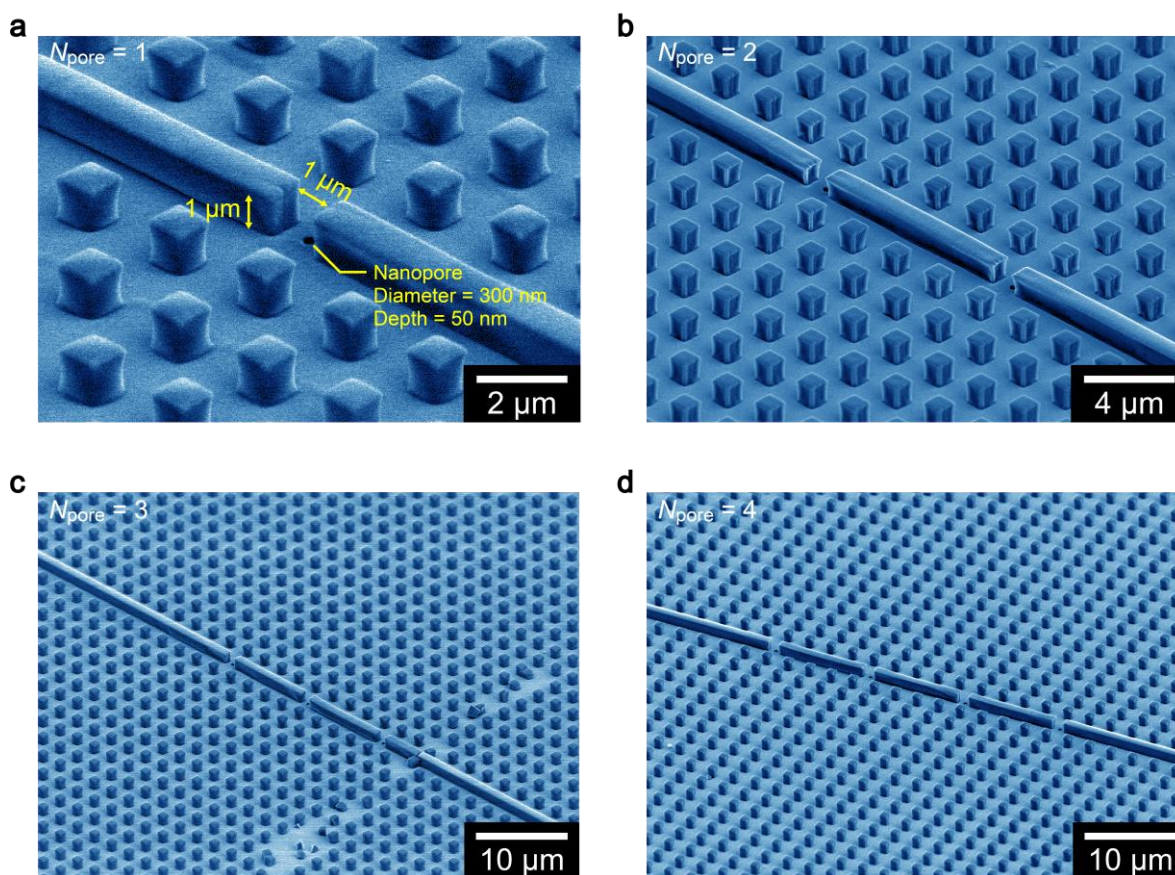
Figure S2. Structure of feed-through channel-integrated nanopores. **a,** Scanning electron micrograph showing a 1 µm-sized channel with a 300 nm-diameter nanopore fabricated on a 50 nm-thick Si_3N_4 membrane. **b-d,** Structures of the multi-microchannel/nanopore sensors with the number of unit N_{pore} of 2 (b), 3 (c), and 4 (d).
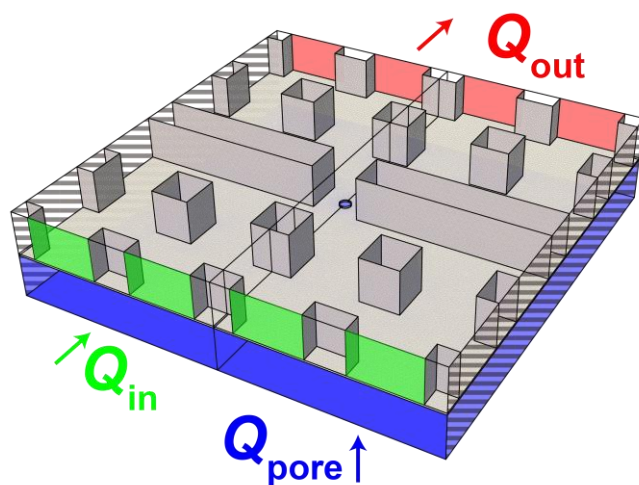
Figure S3. Model structure and boundary conditions used for the finite element analyses. The size of the microchannels and nanopore was deduced from the scanning electron micrographs in Fig. S2. Details are described in Methods section.
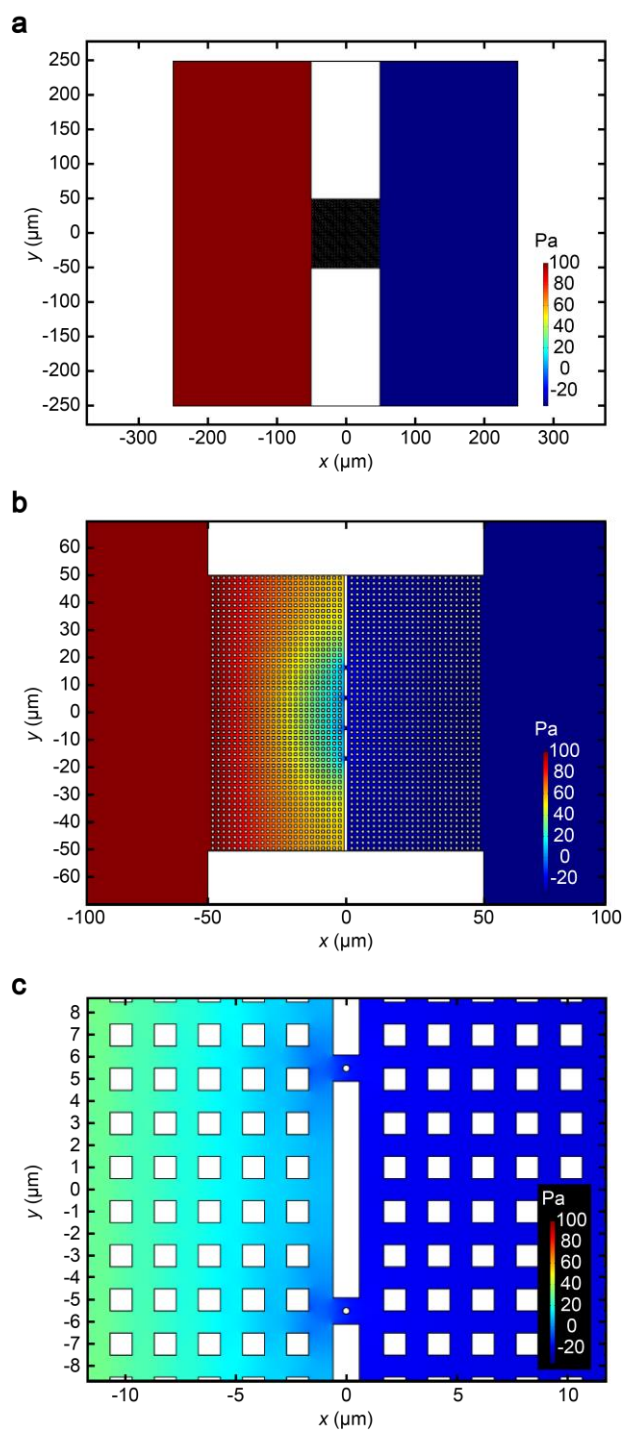
Figure S4. Finite element analysis of pressure distributions in the integrated nanopore. a-c, Top views of the pressure distributions around the microchannel/nanopore structure displayed at different scale; 500 μm x 500 μm (a),

200 µm x 140 µm (b), and 25 µm x 18 µm (c).   It is noticeable that the pressure

drops mostly at the 1 µm height channel.
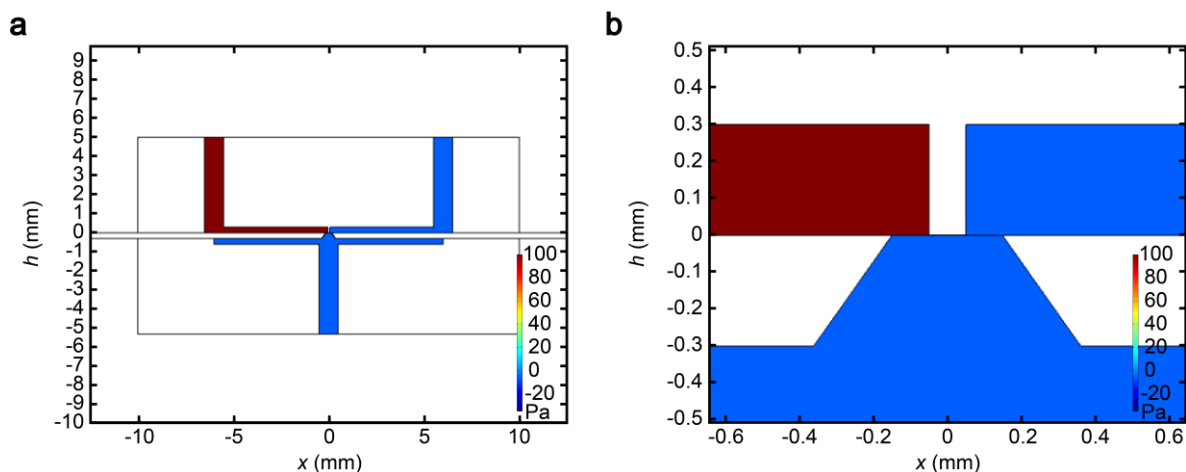
Figure S5.   Finite element analysis of pressure distributions in the integrated nanopore.   a, Two-dimensional pressure profiles in the device.   Left side of the inlet hole in the PDMS block was kept at 10 Pa while the outlet at the right side was set to zero.   The dimensions were defined from the photo- and SEM-images.   The simulations were performed using COMSOL 5.4 that solved Nernst-Plank and Nervier-Stokes equations.   On the nanopore wall surface, negative charge of density of −10 mC/m2 along 50 nm length was added to simulate the electroosmotic flow under the applied potential difference at the inlet and outlet (0.1 V in the calculations).   **b,** Close-up view of (a) at the 1 μm-height channel where most of the applied pressure dropped.
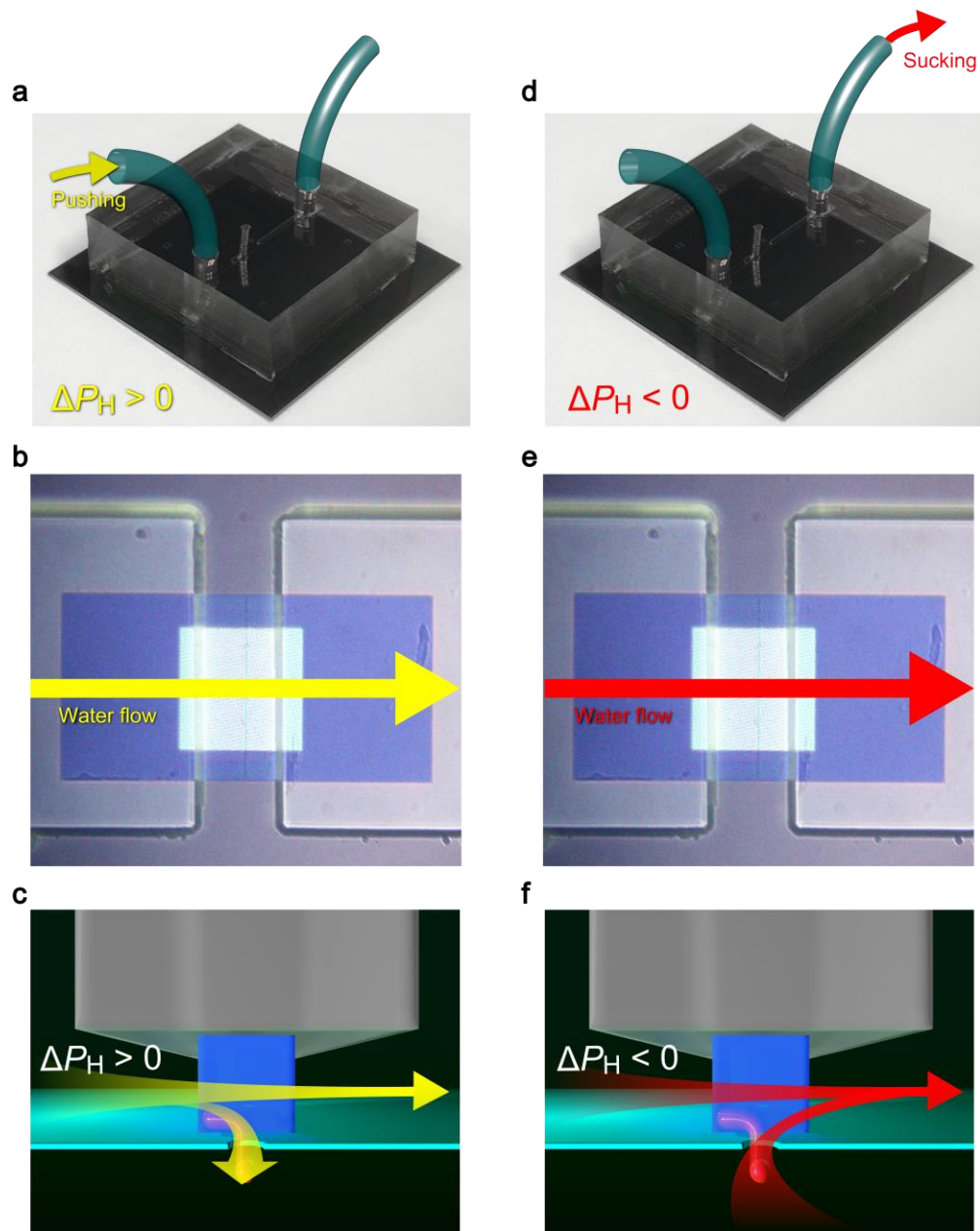
Figure S6. Different sample setup used to apply positive and negative pressure.   a-c, Positive pressure was added through one of the inlet located at the channel upstream.   **d-f,** Negative pressure was loaded through the hole at the

downstream side.　　By this, we kept water flowing in the same direction irrespective
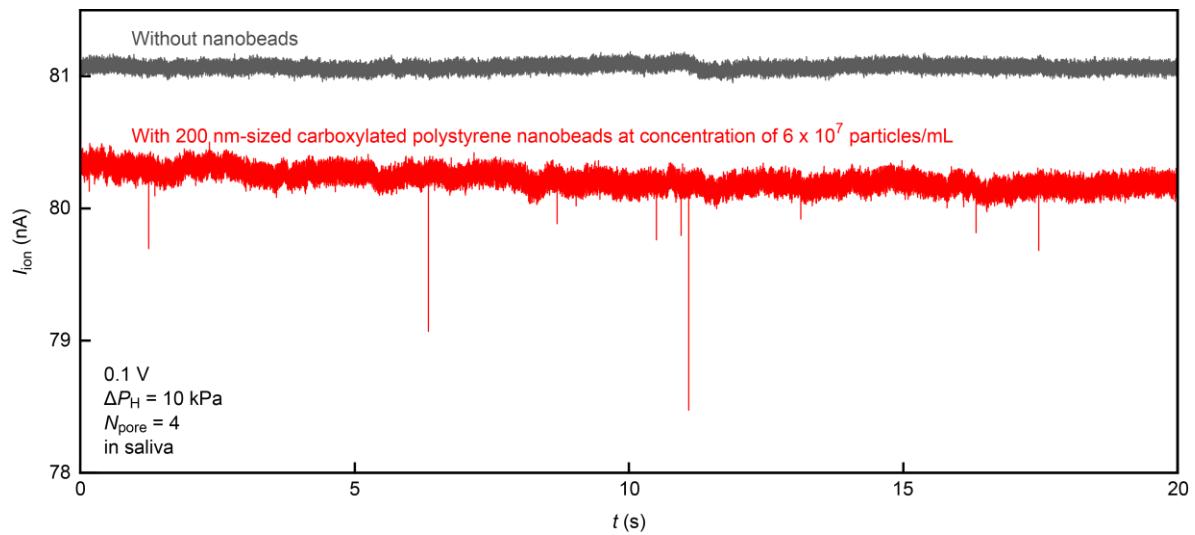
of the sign of the pressure ΔP_H.
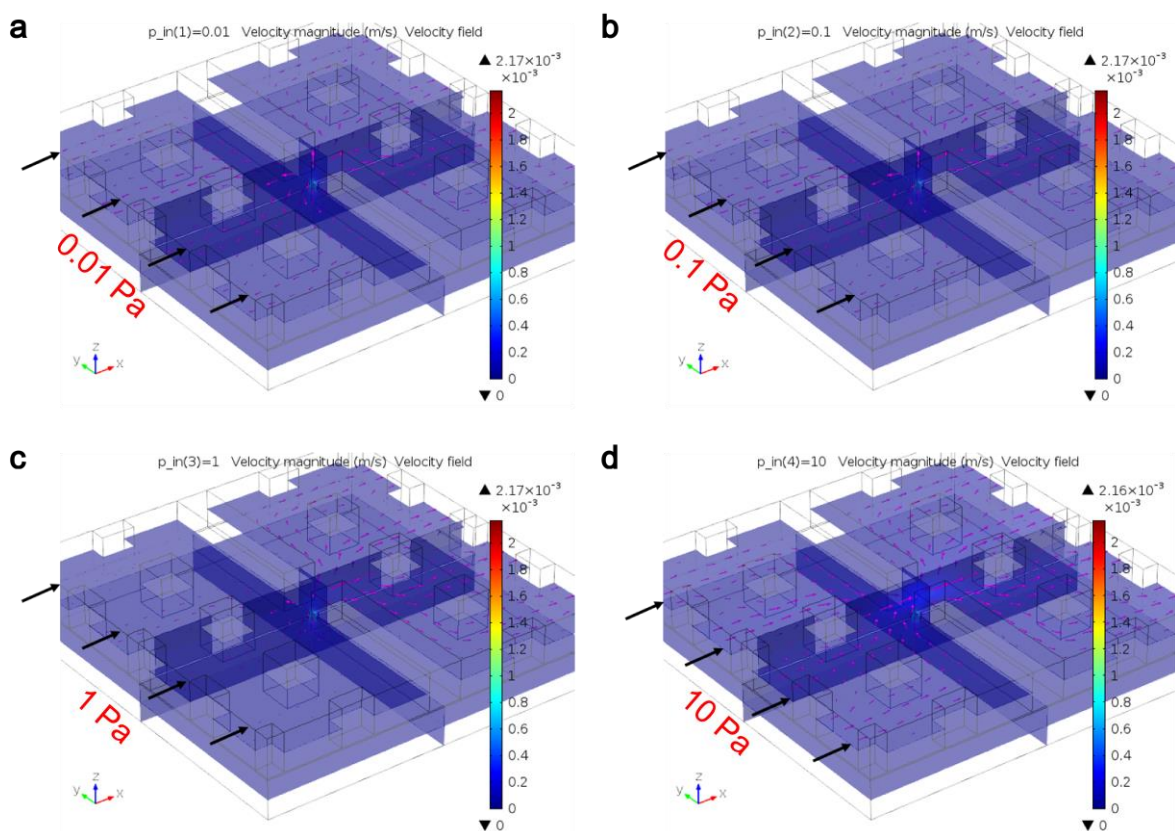
Figure S7. Effects of electroosmotic flow. a-d, Three-dimensional fluid velocity profiles obtained from the COMSOL simulations under various input pressure conditions of 0.01 Pa (a), 0.1 Pa (b), 1 Pa (c), and 10 Pa (d). Potential difference of 0.1 V was also added to consider the electroosmotic flow from the negative native surface charge on the 300 nm-diameter nanopore wall in the 50 nm-thick Si_3N_4 membrane. Arrows points toward the direction of the water flow. When pressure is lower than 10 Pa, the water does not flow along the pressure direction but tends to come out from the 1 μm-sized channel as well as the nanopore due to significant contributions of the electroosmosis.
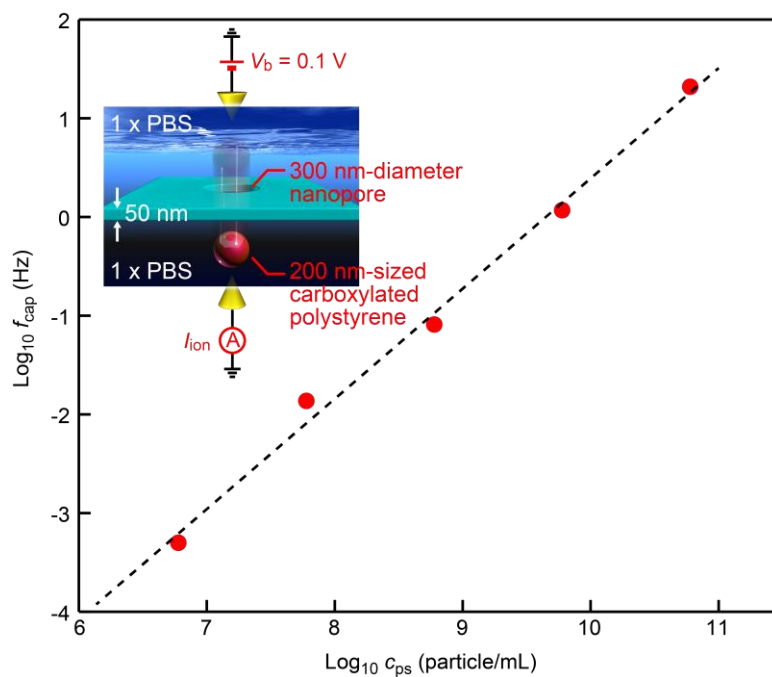
Figure S8. Nanoparticle capture rates in a nanopore. A 300 nm-diameter nanopore in a 50 nm-thick Si_3N_4 membrane was used for resistive pulse measurements in 1 x PBS containing 200 nm-sized carboxylated polystyrene nanoparticles at concentration c_{ps} from 6 x 10^6 to 6 x 10^9 particle/mL under the applied voltage of 0.1 V. Dashed line is linear fit to the plots.
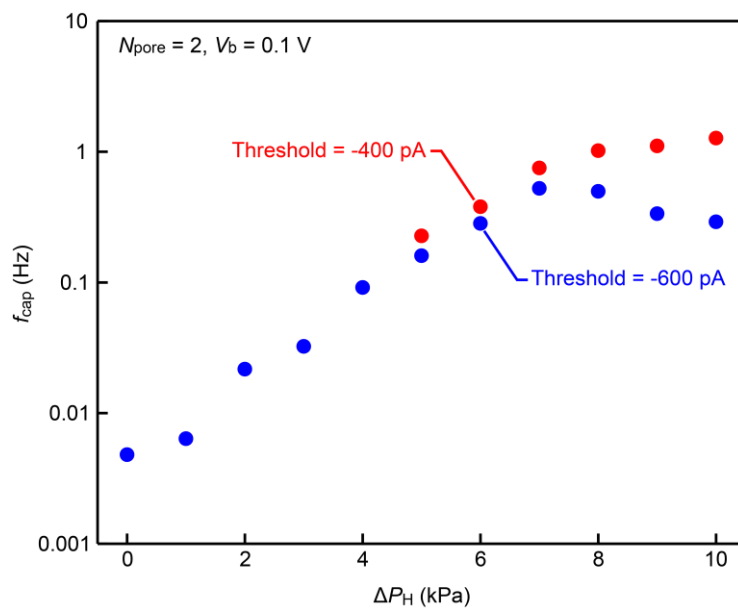
Figure S9. Influence of current threshold on the extracted number of resistive pulses. The capture rates f_{cap} of 200 nm-sized carboxylated polystyrene in 1 x PBS at 6 x 10^8 particle/mL under 0.1 V deduced from the number of pulses counted in the ionic curve with thresholds set to –600 pA (blue) and -400 pA (red). f_{cap} tends to decrease with the applied pressure ΔP_H when using the high threshold level due to existence of larger number of pulses of height smaller than 600 pA under the elevated pressure conditions

Without nanobeads

With 200 nm-sized carboxylated polystyrene nanobeads at concentration of 6 x 10^7 particles/mL

0.1 V
ΔP_H = 10 kPa
N_{pore} = 4
in saliva

Figure S10. Negative control of resistive pulse measurements in saliva.
Ionic current curves in saliva with (red) and without (grey) adding 200 nm-diameter carboxylated polystyrene nanoparticles at a concentration of 6 x 10^7 particles/mL.
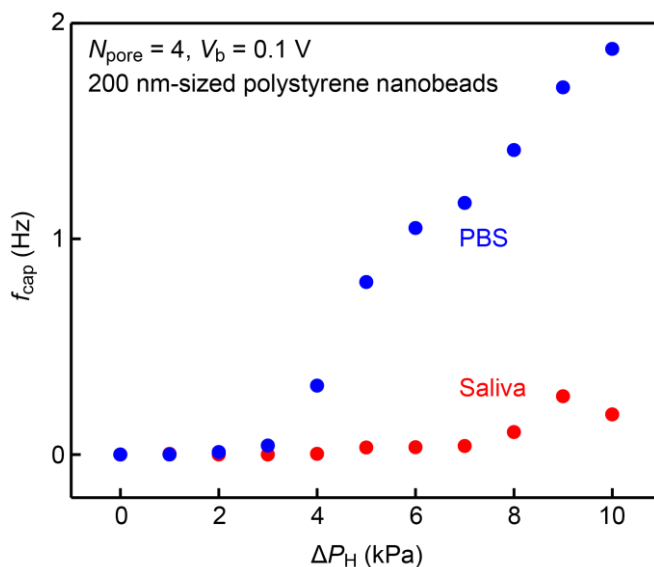
Figure S11. Particle capture efficiency in saliva. Although clinical study is beyond the scope of the present study, it is vital to know whether the fluid feed-through approach is viable in physiological media such as body fluid. We thus verified the medical applicability by extending the ionic current measurements in human saliva that in general consists of 99 % water with miscellaneous chemical and biological components including enzyme and protein molecules such as amylase and mucin. As shown in Fig. S7, resistive pulses were almost completely absent when adding no test particles that would be attributed to electrically-neutral objects (or those having little surface charge) being flown-through the microchannel without being given a chance to enter the nanopore, as suggested by the larger in-plane fluid flow rate (Q_{out}) compared to the cross-membrane counterpart (Q_{pore}) displayed in Fig. 3b. Meanwhile, the open pore current demonstrated fluctuations most likely due to passing-by of various charged nanoscopic molecules through the pore. In contrast, only when adding negatively-charged nanobeads did we

observed significant I_{ion} signals by virtue of the additional electrophoretic forces acting to capture the pressure-driven nanoparticles into the nanopore. This is indeed another outcome of the feed-through method that enable selective detections of specific analytes having enough surface charges in a real biological media. The remaining concern is the influence of the liquid viscosity that caused a factor of 19 decrease in f_{cap} for the case of viscous saliva compared to that in PBS on average by the fact that $Q \sim \Delta P_H/\mu$ as described in Fig. S8 for f_{cap} of 200 nm-sized carboxylated nanobeads in PBS (blue) and human saliva (red) in the integrated channel/nanopore device with the number of pore N_{pore} of 4 under the applied voltage of 0.1 V and pressure ΔP_H. The applied pressure should therefore be optimized to meet practical requirements when dealing with viscous biological fluids.